Multiphoton phosphorescence quenching microscopy reveals kinetics of tumor oxygenation during anti-angiogenesis and angiotensin signaling inhibition

John D. Martin[1,2,a,#], Ryan M. Lanning[1,3,b#], Vikash P. Chauhan[1,4,c], Margaret R. Martin[1,d], Ahmed S. Mousa[1,e], Walid S. Kamoun[1,f], Hee-Sun Han[5,g], Hang Lee[6], Triantafyllos Stylianopoulos[1,h], Moungi G. Bawendi[5], Dan G. Duda[1], Edward B. Brown[1,i], Timothy P. Padera[1], Dai Fukumura[1], Rakesh K. Jain[1,*]

Affiliations:

[1]*Edwin L. Steele Laboratories, Department of Radiation Oncology, Massachusetts General Hospital, Harvard Medical School, Boston, MA*

[2]*Department of Chemical Engineering, Massachusetts Institute of Technology, Cambridge, MA*

[3]*Harvard-Massachusetts Institute of Technology Division of Health Sciences and Technology, Cambridge, MA*

[4]*School of Engineering and Applied Sciences, Harvard University, Cambridge, MA*

[5]*Department of Chemistry, Massachusetts Institute of Technology, Cambridge, MA*

[6]*Biostatistics Center, Harvard Medical School, Massachusetts General Hospital, Boston, MA*

[#]*These authors contributed equally*

[*] *Correspondence to*

jain@steele.mgh.harvard.edu (RKJ)

[a]*Present address: NanoCarrier Co., Ltd., Tokyo, Japan*

[b]*Present address: Department of Radiation Oncology, School of Medicine, University of Colorado, Aurora, CO*

[c]*Present address: Koch Institute for Integrative Cancer Research, Massachusetts Institute of Technology, Cambridge, MA*

[d]*Present address: Department of Computer Science, Tufts University, Medford, MA*

[e]*Present address: Pieris Pharmaceuticals, Inc., Boston, MA*

[f]*Present address: Takeda Oncology, Cambridge, MA*

[g]*Present address: Department of Chemistry, University of Illinois, Urbana, IL*

[h]*Present address: Cancer Biophysics Laboratory, Department of Mechanical and Manufacturing Engineering, University of Cyprus, Nicosia, Cyprus*

[i]*Present address: Department of Biomedical Engineering, University of Rochester, Rochester, NY*

Supplementary Tables

Supplementary Table 1 – Mean and maximum distance (μm) to nearest vessel in normal tissue

	Skin – mice breathing air	Skin – mice breathing 100% oxygen	Bone marrow single vessel cavities	Bone marrow endosteal regions
Mean	24.7 μm	24.2 μm	13.5 μm	11.2 μm
Max	83.9 μm	83.9 μm	58.4 μm	45.8 μm

Supplementary Table 2 – Mean and maximum distance (μm) to nearest vessel in tumors

	U87	LS174T	MCaIV	E0771
Mean	39.6 μm	49.4 μm	53.3 μm	50.6 μm
Max	61.6 μm	232 μm	300 μm	412 μm

Supplementary Table 3 – High-dose DC101 MCaIV Day 0 – Day 2 – Day 5 response trajectory of extravascular oxygenation linear multiple regression analysis parameters

Variable	Estimate	p-value
Intercept	28.26	<0.0001
Day	-2.800	<0.0001
Treatment	-0.2698	0.8304
Day×treatment	0.9312	0.0241

Supplementary Table 4 – Low-dose DC101 E0771 Day 0 – Day 2 response trajectory of intravascular oxygenation linear multiple regression analysis parameters

Variable	Estimate	p-value
Intercept	38.49	<0.0001
Day	-4.064	0.0477
Treatment	-5.054	0.1445
Day×treatment	7.779	0.0012

Supplementary Table 5 – Low-dose DC101 E0771 Day 0 – Day 2 response trajectory of extravascular oxygenation linear multiple regression analysis parameters

Variable	Estimate	p-value
Intercept	21.48	<0.0001
Day	-1.853	0.0049
Treatment	-11.20	0.0070
Day×treatment	3.850	0.0002

Supplementary Table 6 – Losartan E0771 Day 2 – Day 5 response trajectory of extravascular oxygenation linear multiple regression analysis parameters

Variable	Estimate	p-value
Intercept	21.48	<0.0001
Day	-1.853	0.0049
Treatment	-11.20	0.0070
Day×treatment	3.850	0.0002

Supplementary Figures

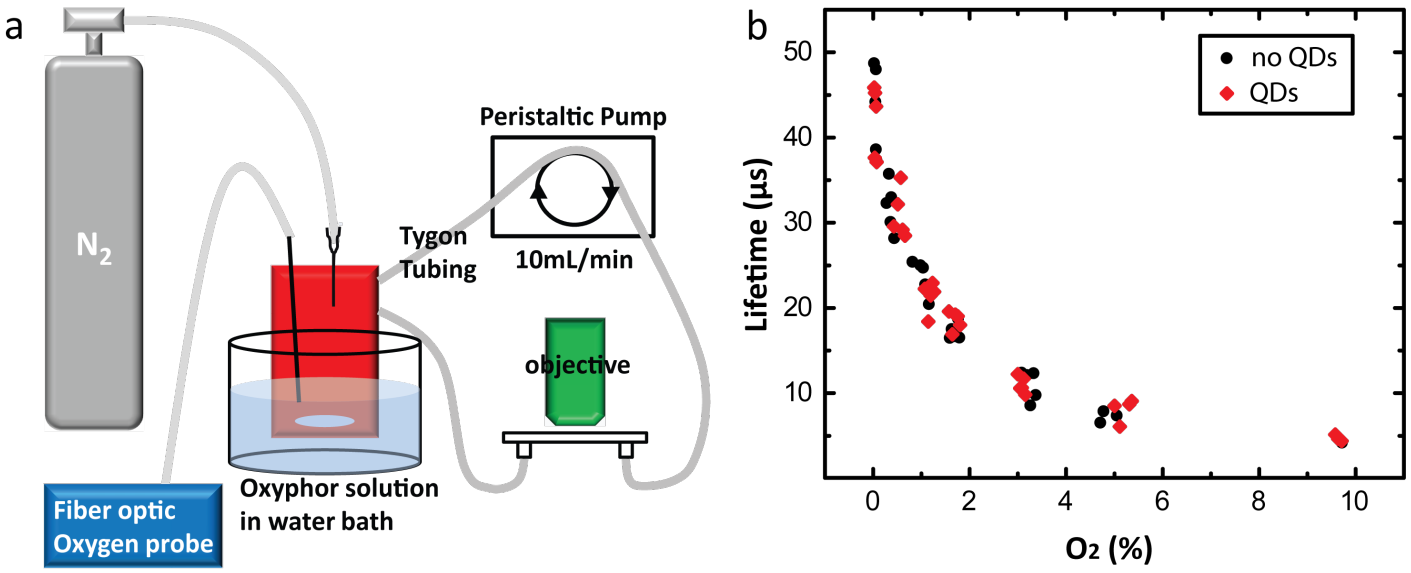

Supplementary Figure 1 – Quantum dots do not affect system calibration. (a) Diagram of the recirculating, sealed calibration system employing a fiber oxygenator indicating the direction of fluid and gas flow. An independent pO_2 measurement is made with an optical fiber ruthenium-based probe. (b) Lifetime of phosphorescence as a function of oxygen concentration in the albumin solution (black dots) and with quantum dots (QDs) added (red dots).

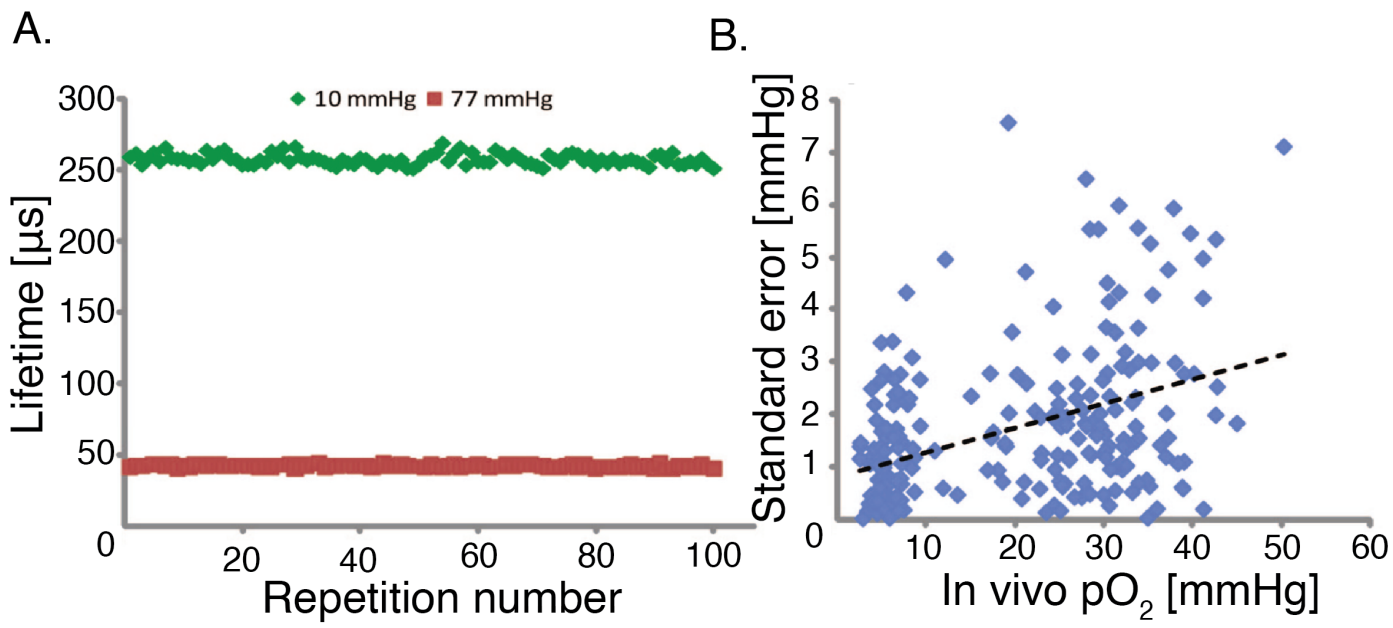

Supplementary Figure 2 –Reproducibility and variability as a function of oxygen tension. (a) A graph of repeated phosphorescence lifetime measurements *in vitro* at 11 mmHg (green) and 77 mmHg (red) oxygen tension. (b) A graph of the standard error of *in vivo* oxygen tension measurements as a function of oxygen tension. The dashed line depicts the correlation with a Pearson's correlation coefficient of 0.41.

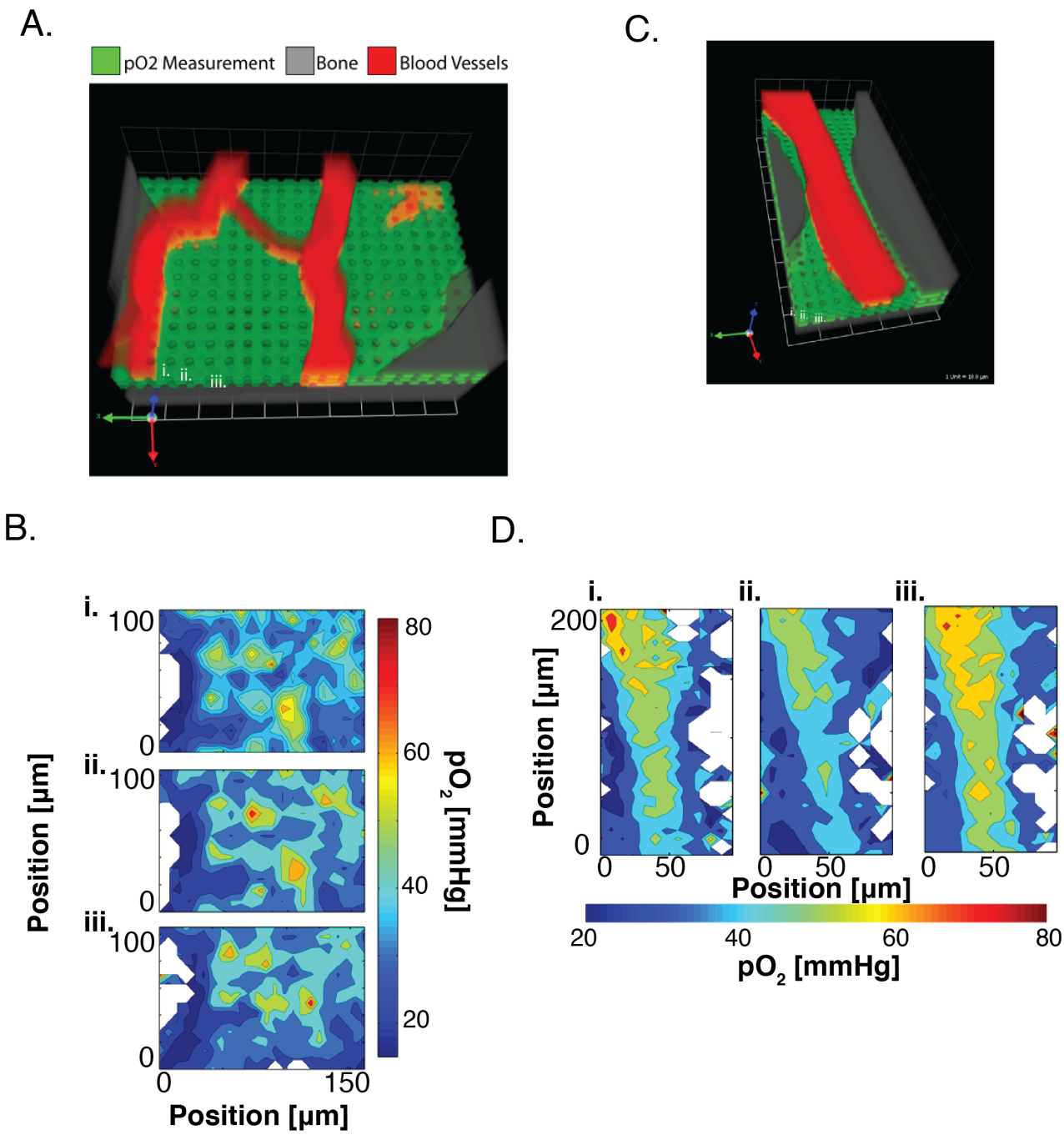

Supplementary Figure 3 – Measurement of pO_2 in murine bone marrow. (a) Map of vessels (red) and locations of oxygen measurements (indentions in green area) in the calvarial bone marrow in a cavity with multiple vessels. (b) Three maps of oxygen measurements in the region shown in (a) at different z depths (i, ii and iii). (c) Map of a vessel (red) and locations of oxygen measurements (indentions in green area) in the calvarial bone marrow in a cavity with a single endosteal vessel. (d) Three maps of oxygen measurements in the region shown in (c) at different z depths (i, ii and iii).

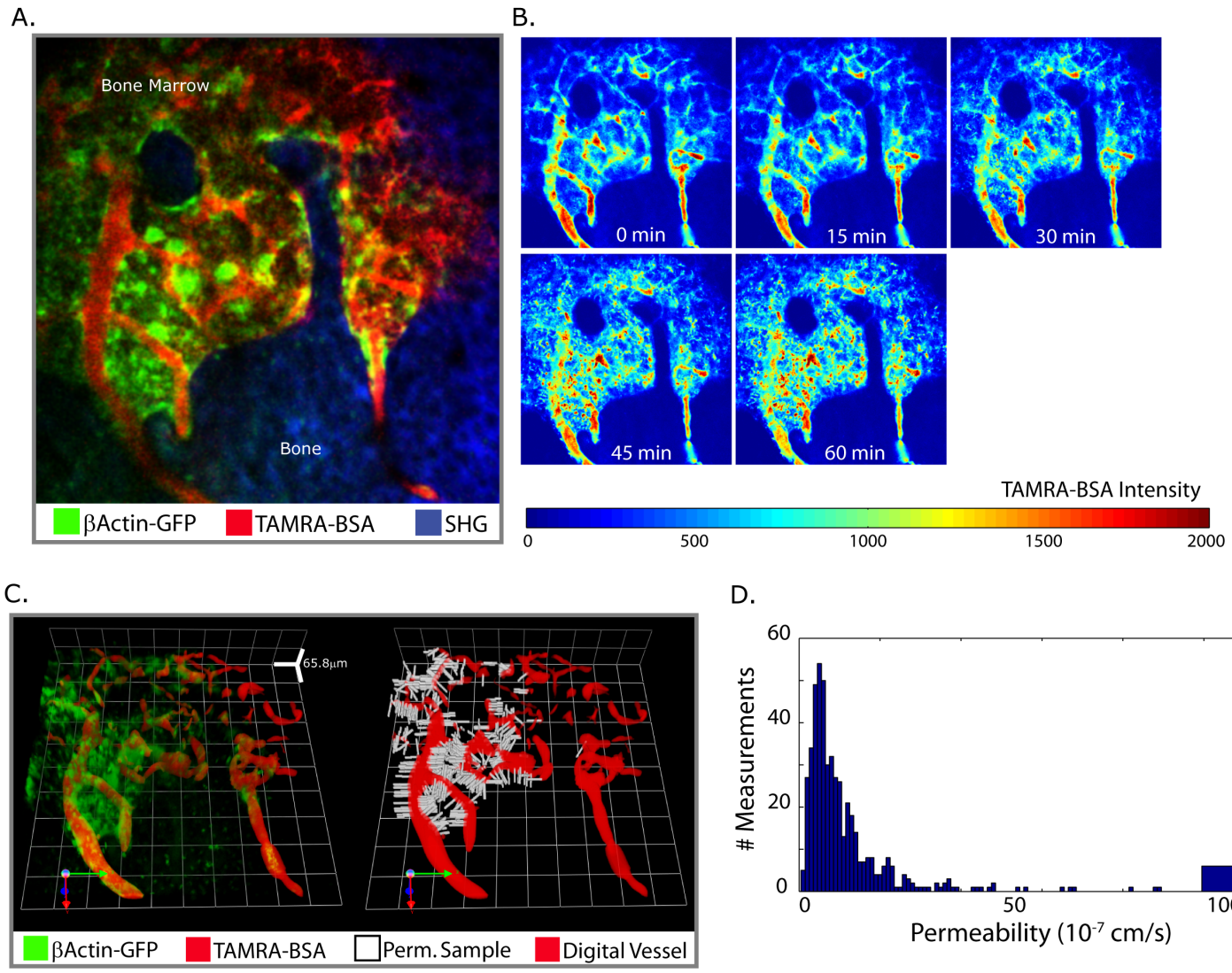

Supplementary Figure 4 – Bone marrow vessels are hyperpermeable to albumin. (a) Representative image of the bone marrow after injection of rhodamine albumin (TAMRA-BSA - red) in an Actb-GFP mouse (bone marrow cells are shown in green, and the bone in blue – by second harmonic generation) using intravital multi- photon microscopy. (b) TAMRA-BSA intensity heat map showing extravasation of albumin over time, which is detectable within 15 and 30 minutes after i.v. injection. (c) Analysis of effective vessel permeability. Vessels are segmented and perpendicular gradient paths are randomly selected in 3-D. BSA accumulation is quantified along each path and effective permeability calculated from the fluorescent gradient. (d) Histogram of effective permeability quantified along spots along the vessel wall surface.

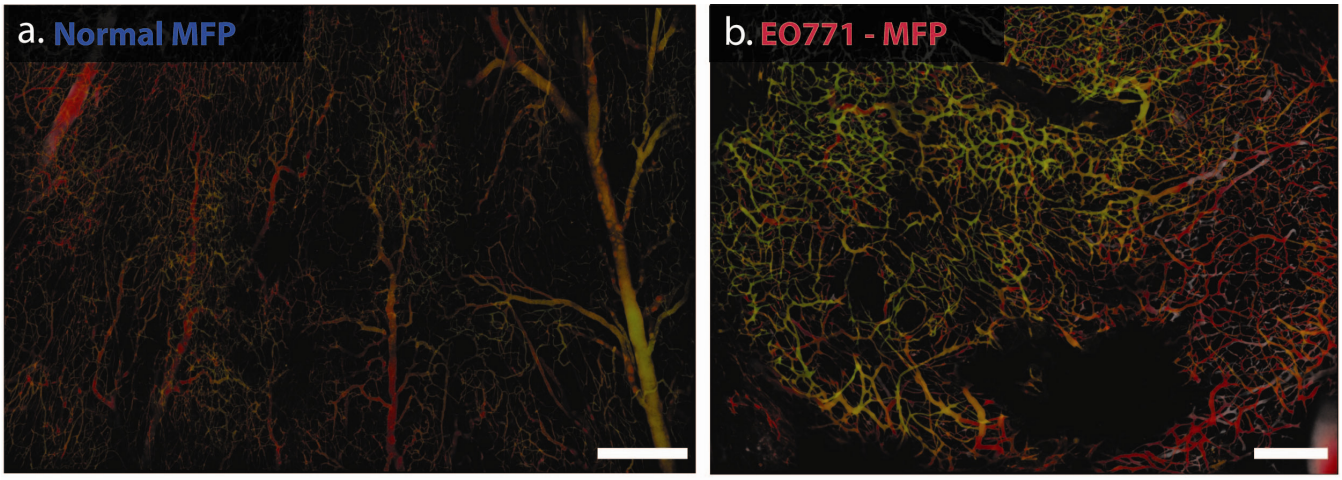

Supplementary Figure 5 – Tumor vessels are abnormal. (a) Angiographic depth projection of the vasculature in the normal mammary fat pad (MFP) of a female SCID mouse. (b) Angiographic depth projection of the vasculature in a murine mammary carcinoma (EO771) implanted in the MFP. Color denotes depth (green red white). Scale Bars 500 μm.

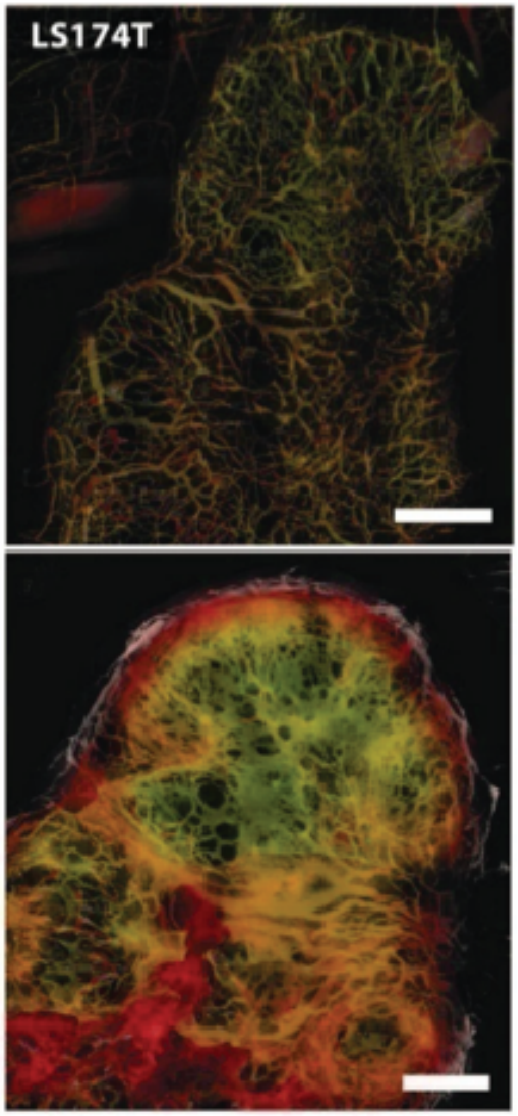

Supplementary Figure 6 – Comparison of a LS174T tumor vascular network at the first imaging of the tumor (*top*) and nine days later (*bottom*). Images are presented as colorized depth projections (superficial to deep: green red white). Scale Bars 500 μm.

A.

Correlation of pO_2 and diameter	U87	LS174T	MCaIV	E0771
Coefficient	0.101	0.0466	0.326	-0.0131
p-value	0.44	0.26	1.3E-07	0.85

B.

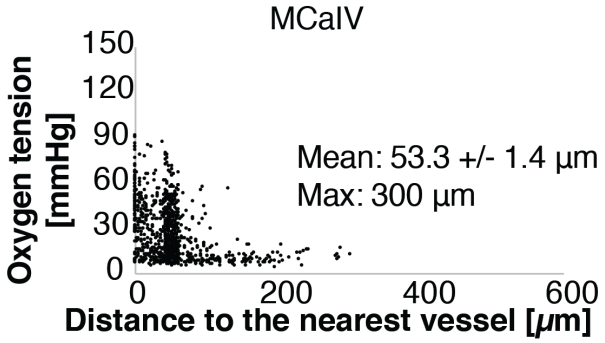

C.

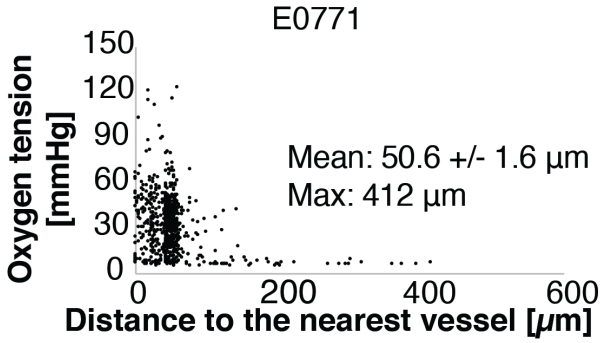

D.

Correlation of pO_2 and distance	U87	LS174T	MCaIV	E0771
Coefficient	-0.0197	-0.074	-0.299	-0.291
p-value	0.85	0.025	2.3E-14	7.8E-14

Supplementary Figure 7 – Simultaneous angiography and oxygen tension measurements reveal abnormal function of tumor vessels and the dependence of oxygen tension on distance to the nearest vessel. (a) Table of Pearson correlation coefficients and the p-value of the correlation of oxygen tension and nearest vessel diameter. (b) Scatter plot of measured oxygen tension versus the distance to the nearest vessel in MCaIV tumors. The maximum and mean distances to the nearest vessel and the standard error of the means are displayed in the graph. (c) Scatter plot of measured oxygen tension versus the distance to the nearest vessel in E0771 tumors. The maximum and mean distances to the nearest vessel and the standard error of the means are displayed in the graph. (d) Table of Pearson correlation coefficients and the p-value of the correlation of oxygen tension and distance to the nearest vessel.

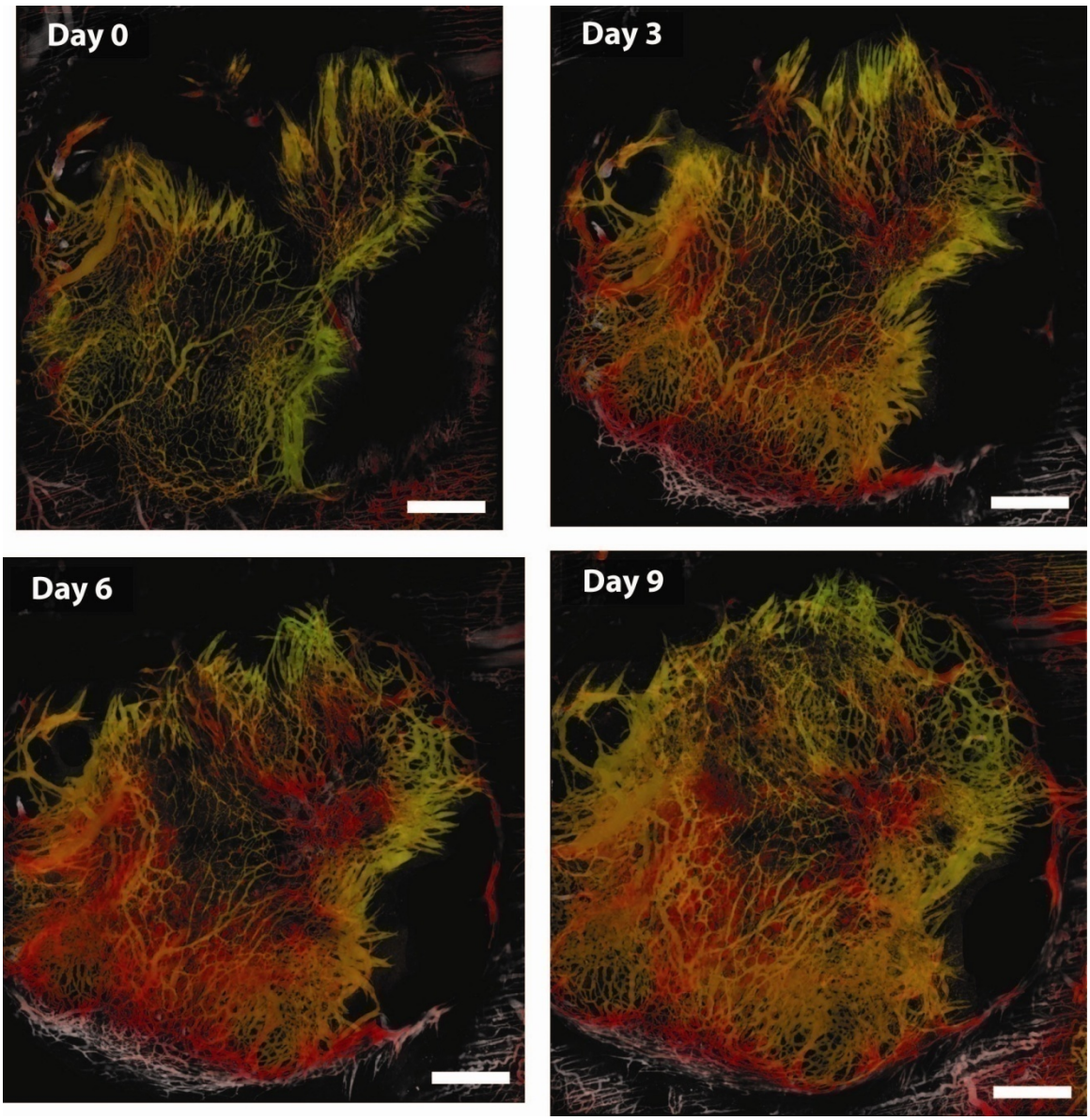

Supplementary Figure 8 – Angiogenesis during tumor growth. The vasculature of an LS174T colorectal adenocarcinoma xenograft is shown over 9 days. Increased angiogenesis is notable throughout tumor growth. Tumor vasculature is presented as a colorized maximum intensity depth projection (superficial to deep: green red white). Scale Bars 500 μm.

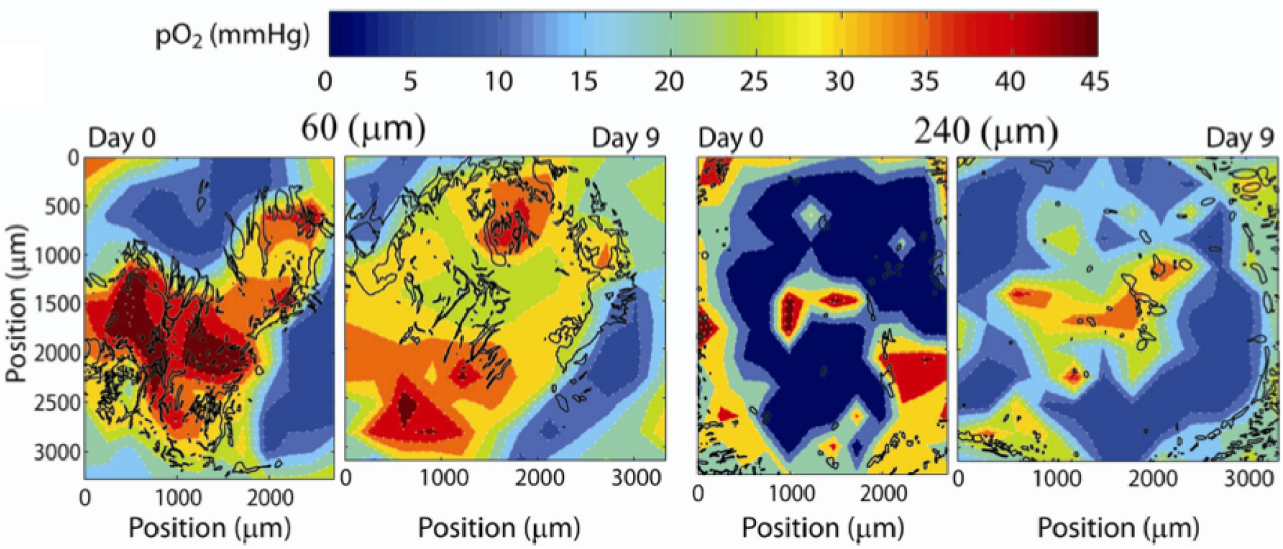

Supplementary Figure 9 – Depth gradients in pO2 during LS174T tumor growth. Oxygen tension maps at 60 and 240 μm in the tumor on the first day of imaging and nine days later. Vascular casts from either 60 or 240 μm depths from the angiographic imaging overlay the oxygen heat maps.

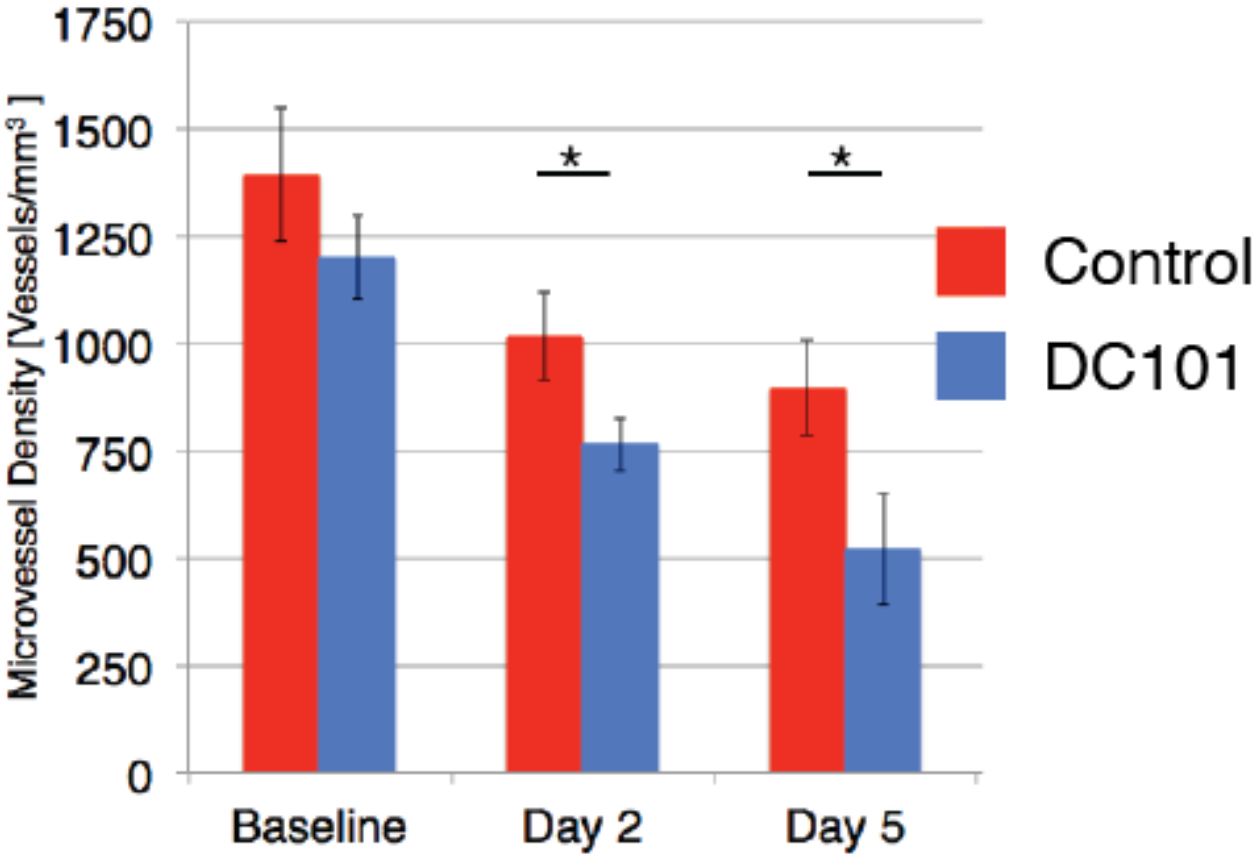

Supplementary Figure 10 – Bar graph indicating the perfused microvessel density of E0771 control IgG and high-dose DC101 treated tumors. Control and treated tumors at each timepoint were compared using Student's t-test, with an asterisk (*) denoting a p-value less than 0.05. Error bars represent standard error of the mean. N = 5 mice per group.

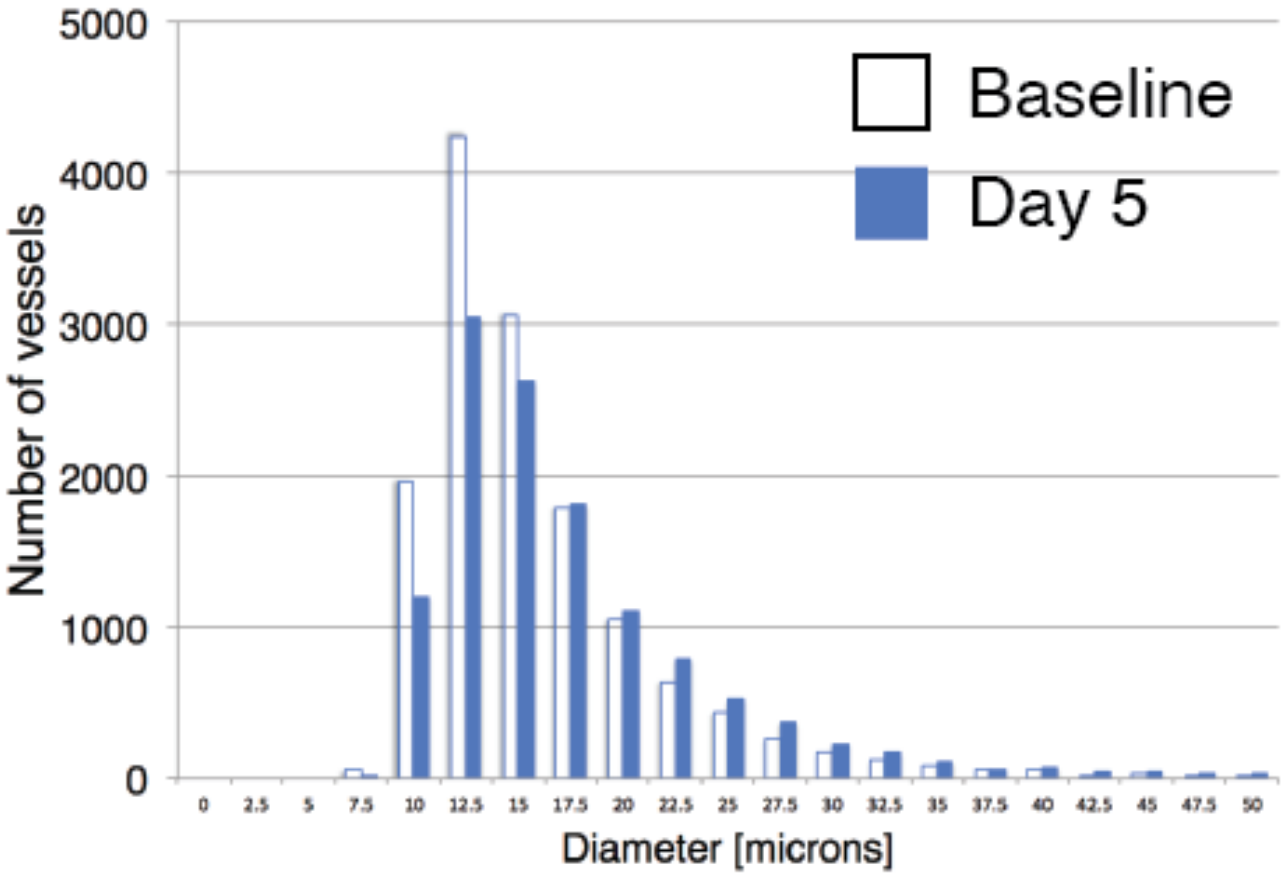

Supplementary Figure 11 – Histogram of E0771 tumor vessel diameters in high-dose DC101-treated mice at baseline (white bars) and at Day 5 (blue bars).

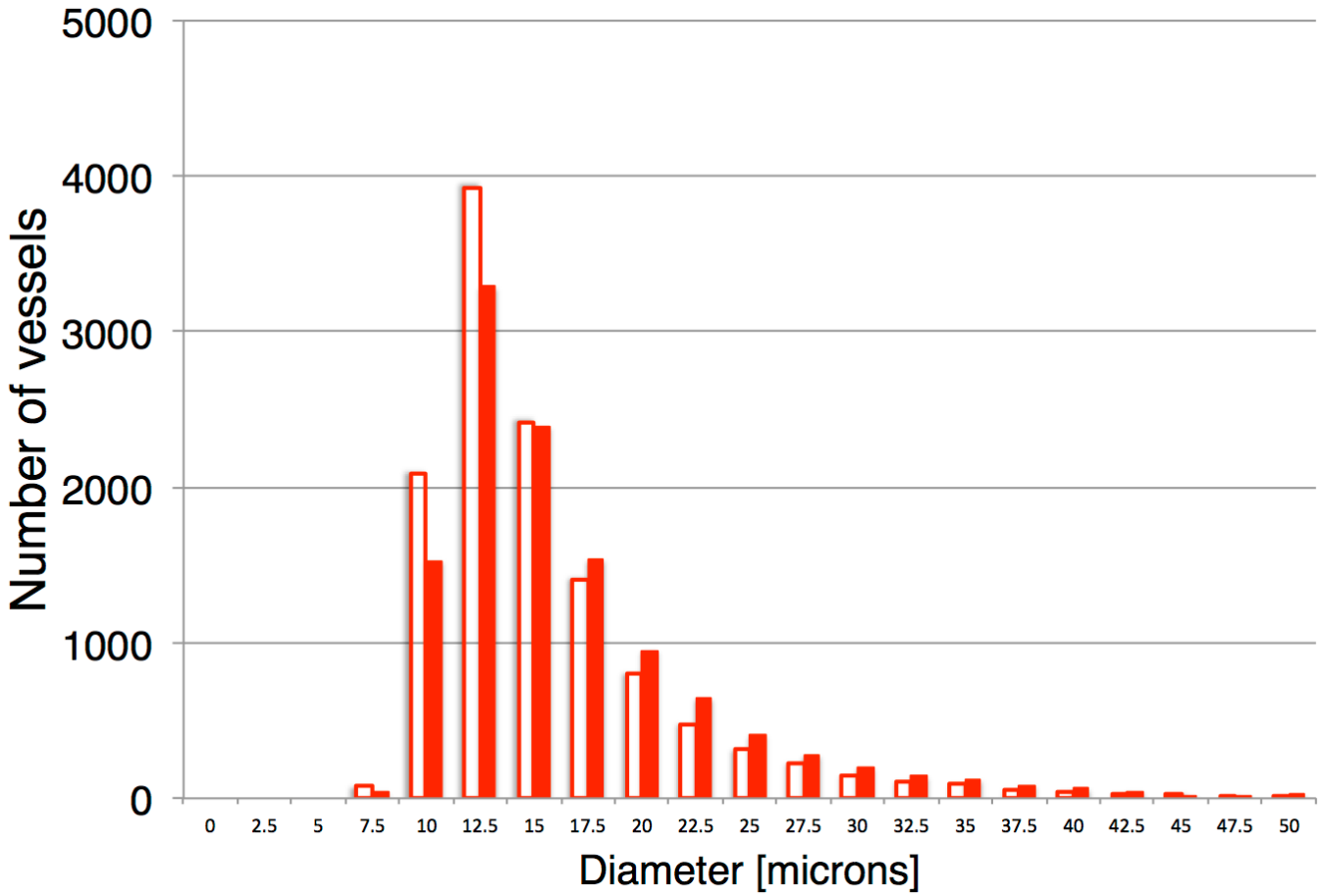

Supplementary Figure 12 – Histogram of E0771 tumor vessel diameters in control IgG-treated mice from the high-dose DC101-treated experiment at baseline (white bars) and at Day 5 (red bars).

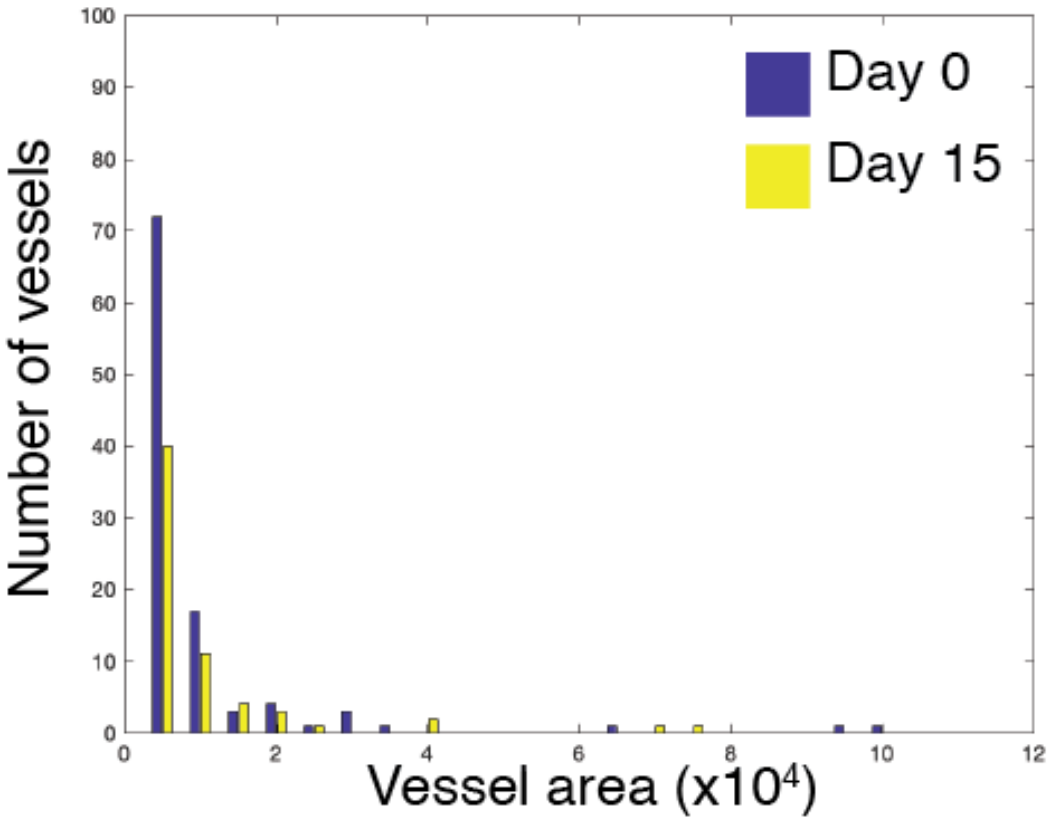

Supplementary Figure 13 – Distribution of vessel sizes in a representative breast cancer patient treated with bevacizumab. Patient selected from a previously reported study (1).

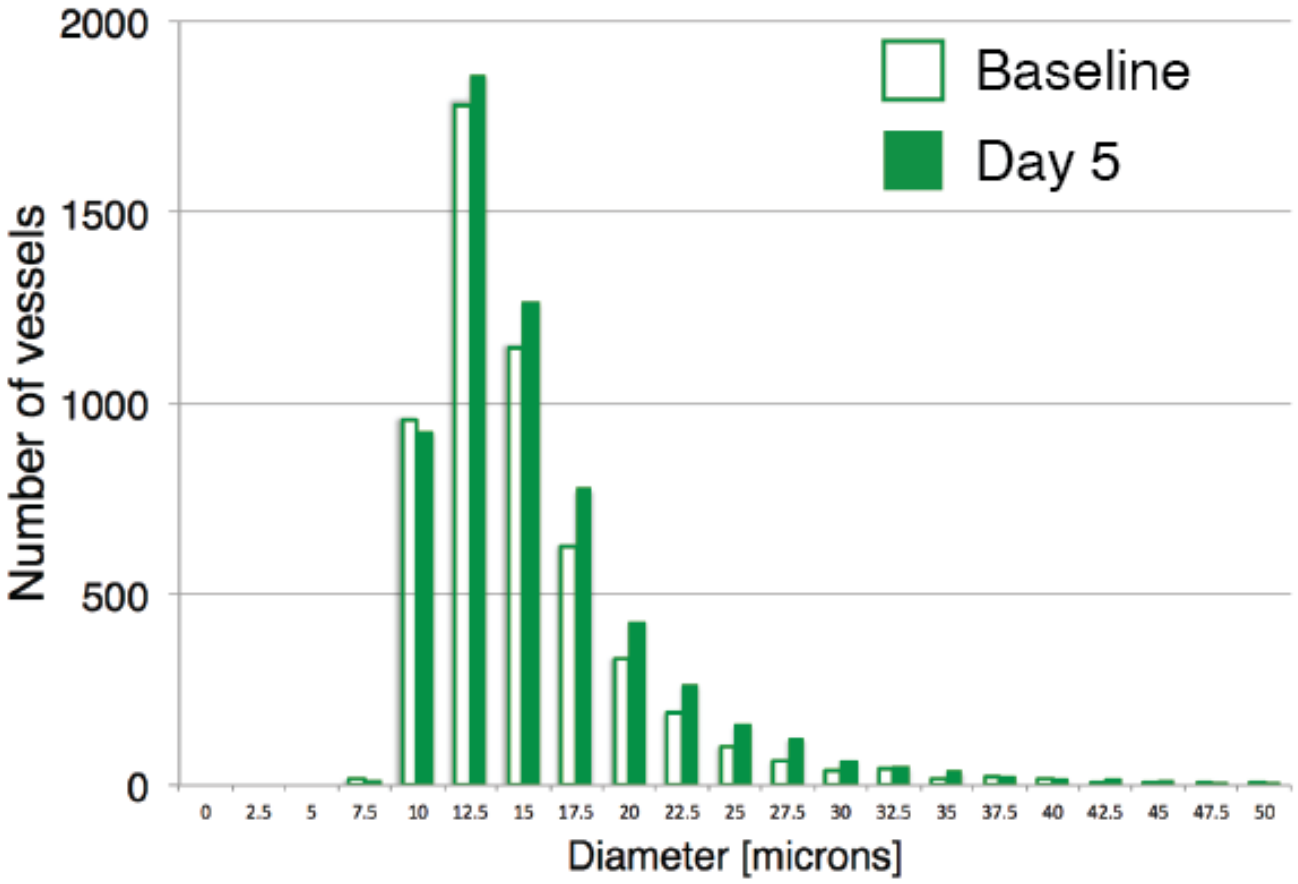

Supplementary Figure 14 – Histogram of vessel diameters in losartan treated mice bearing E0771 tumors at baseline and at Day 5.

Supplementary Methods

Real time intravital microscopy in the intact bone marrow allows characterization of vessel structure and function. Because previous PQM measurements were based on the infusion of nano-constructs into the bone marrow (2), we first characterized the transvascular transport of these macromolecules within the bone marrow. Analysis of the structure of the bone marrow vasculature showed the presence of a characteristic sinusoidal capillary network. Direct quantification of the extravasation rate of macromolecules in these vessels revealed a significant extravasation of macromolecules as high as MW 500 kDa. To quantify the rate of extravasation of macromolecules, we performed intravital multiphoton microscopy of the bone marrow before and at several time points after injection of TAMRA-BSA. We quantified vascular permeability at multiple positions along the vessel wall surface using a method previously developed by our group (3). BSA extravasated within few minutes and accumulated in the bone marrow (Supplementary Figure 2). Median permeability was 7.6 [25 percentile = 4.6, 75 percentile = 13.1] $\times 10^{-7}$ cm/s. These high values are comparable to the permeability previously measured in tumor vessels (4-11) and in bone marrow sinusoids (12-14) and are substantially higher than vascular permeability measured in normal skin or brain.

Supplementary Discussion

MCaIV has small vessels surrounded by ~100 μm cancer cell sleeves interspersed with necrotic regions. The oxygen consumption by cancer cells around small vessels results in low interstitial oxygen around small vessels. In contrast, there are also some large vessels in the tumor periphery (11) and others with a 20 μm region of stroma separating the vessel and cancer cells (15). These narrow regions of stroma surrounding large vessels may have less oxygen consumption resulting in relatively high interstitial oxygen levels. This is a potential explanation for the correlation of vessel radius and interstitial oxygenation observed in MCaIV that is not characteristic of most tumors.

References

1. S. M. Tolaney *et al.*, Role of vascular density and normalization in response to neoadjuvant bevacizumab and chemotherapy in breast cancer patients. *Proceedings of the National Academy of Sciences* **112**, 14325-14330 (2015).
2. J. A. Spencer *et al.*, Direct measurement of local oxygen concentration in the bone marrow of live animals. *Nature* **508**, 269 (2014).
3. E. B. Brown *et al.*, In vivo measurement of gene expression, angiogenesis and physiological function in tumors using multiphoton laser scanning microscopy. *Nature medicine* **7**, 864-868 (2001).
4. F. Yuan *et al.*, Time-dependent vascular regression and permeability changes in established human tumor xenografts induced by an anti-vascular endothelial growth factor/vascular permeability factor antibody. *Proceedings of the National Academy of Sciences* **93**, 14765-14770 (1996).
5. F. Yuan *et al.*, Vascular permeability in a human tumor xenograft: molecular size dependence and cutoff size. *Cancer Research* **55**, 3752-3756 (1995).
6. F. Yuan *et al.*, Vascular permeability and microcirculation of gliomas and mammary carcinomas transplanted in rat and mouse cranial windows. *Cancer Research* **54**, 4564-4568 (1994).
7. F. Yuan, M. Leunig, D. A. Berk, R. K. Jain, Microvascular permeability of albumin, vascular surface area, and vascular volume measured in human adenocarcinoma LS174T using dorsal chamber in SCID mice. *Microvasc Res* **45**, 269-289 (1993).
8. M. Dellian, F. Yuan, V. S. Trubetskoy, V. P. Torchilin, R. K. Jain, Vascular permeability in a human tumour xenograft: molecular charge dependence. *Br J Cancer* **82**, 1513-1518 (2000).
9. D. Fukumura, F. Yuan, M. Endo, R. K. Jain, Role of nitric oxide in tumor microcirculation. Blood flow, vascular permeability, and leukocyte-endothelial interactions. *The American journal of pathology* **150**, 713 (1997).
10. W. L. Monsky *et al.*, Role of host microenvironment in angiogenesis and microvascular functions in human breast cancer xenografts: mammary fat pad versus cranial tumors. *Clin Cancer Res* **8**, 1008-1013 (2002).
11. R. T. Tong *et al.*, Vascular normalization by vascular endothelial growth factor receptor 2 blockade induces a pressure gradient across the vasculature and improves drug penetration in tumors. *Cancer research* **64**, 3731-3736 (2004).
12. D. Passaro *et al.*, Increased vascular permeability in the bone marrow microenvironment contributes to disease progression and drug response in acute myeloid leukemia. *Cancer Cell* **32**, 324-341. e326 (2017).
13. K. Vandoorne *et al.*, Imaging the vascular bone marrow niche during inflammatory stress. *Circulation research* **123**, 415-427 (2018).
14. T. Itkin *et al.*, Distinct bone marrow blood vessels differentially regulate haematopoiesis. *Nature* **532**, 323 (2016).
15. H. Hashizume *et al.*, Openings between defective endothelial cells explain tumor vessel leakiness. *The American journal of pathology* **156**, 1363-1380 (2000).